Rarefaction waves in dusty gases

1988 Fluid Dyn. Res. 4 229

(http://iopscience.iop.org/1873-7005/4/4/A01)

Fluid Dynamics Research 4 (1988) 229–238
North-Holland

Rarefaction waves in dusty gases

T. ELPERIN, O. IGRA and G. BEN-DOR

Pearlstone Center for Aeronautical Engineering Studies, Department of Mechanical Engineering, Ben-Gurion University of the Negev, Beer Sheva, Israel

Received 16 February 1988

Abstract. The propagation of normal rarefaction waves in dusty gases has been investigated numerically, using the modified random choice method with operator splitting technique. The effects of the dust parameters on the flow properties inside and behind the rarefaction wave are studied. The results are compared with those appropriate to a dust-free gas.

1. Introduction

The interest in the gas-dynamic behaviour of a gas–particle suspension grew during the past decades due to its application in many engineering problems. Some typical examples are: metallized propellents of rockets, jet-type dust collectors and blast waves in dusty atmospheres. In addition, mixtures with gases heavily laden with solid particles occur frequently in industrial processes such as plastics manufacturing, flour milling, coal-dust conveying, powder metallurgy and powdered-food processing. General descriptions of such flows can be found in several books and review papers (Soo 1967, Marble 1970, Rudinger 1973). Rarefaction waves are a common feature of nonstationary gas flows encountered in engineering practice and research. They appear in the piping system of reciprocating engines and pumps, in gas transportation pipelines and in various shock tubes and blast wave simulators.

When the rarefaction wave propagates into a dust-free gas (sometimes referred to in the literature as a pure gas) the evaluation of the flow properties through and behind it is relatively simple and is well known. For details, see Bannister and Mucklow (1948); Oppenheim, Urtiew and Laderman (1964); Rudinger (1969). These solutions are based on the method of characteristics. A more effective numerical technique, which is especially suitable for handling flow discontinuities (such as shock waves and contact surfaces), is the random-choice method (Chorin 1976, Sod 1977). Igra and Gottlieb (1985) have used this method for studying the interaction of rarefaction waves with area enlargement in ducts.

The purpose of the present paper is to study the case of a rarefaction wave propagating into a dust–gas suspension. In order to evaluate the effect of the presence of the dust and its physical properties on the suspension flow through the rarefaction wave, the numerical solution was performed for different dust loading ratios, different diameters and specific heat capacities of the dust particles. The geometry of the considered flow field is shown schematically in fig. 1. At time $t = 0$ the gas is contained inside a duct and is separated by a diaphragm. The dust-free gas is contained on the left side of the diaphragm while the gas on its right side is uniformly seeded with spherical dust particles of equal diameter. The pressure and the temperature of the dusty gas are higher than those of the pure gas. Originally ($t = 0$) the entire flow system is at rest. After the diaphragm rupture (at $t > 0$), the wave system shown in fig. 1, for $t > 0$, develops. A rarefaction wave R propagates into the high pressure dusty gas region (region 4), and a normal shock wave propagates, in the opposite direction, into the low pressure dust-free

0169-5983/88/$3.50

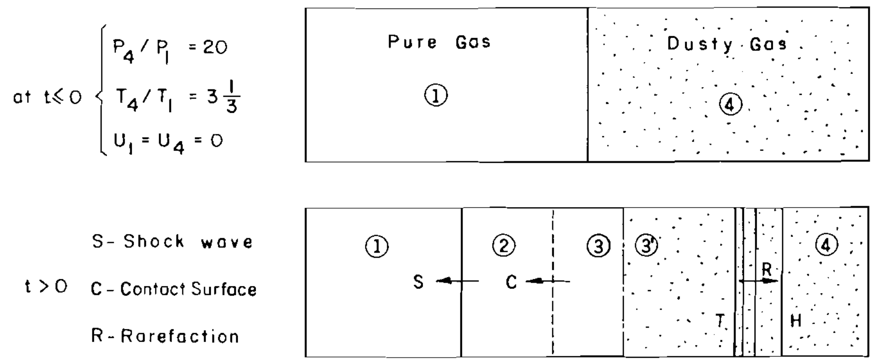

Fig. 1. A schematical illustration of the problem at hand, and the initial conditions used throughout the present numerical study.

gas zone (region 1). A contact surface C separates the gases which were originally separated by the diaphragm. The gas in region 2 was originally in the low pressure side of the diaphragm and the gas in regions 3 and 3′ was originally in the higher pressure side of the diaphragm. Since the solid particles cannot reach the contact surface as they lag behind the gas accelerating them, a dust-free region with a finite length is obtained behind the contact surface. It is of interest to note that Miura and Glass (1982) considered the opposite situation. In their solution the high pressure zone (region 4) was free of dust, while the low pressure zone (region 1) was uniformly seeded with spherical dust particles of equal diameter. Thus, while their study aimed at investigating a dusty shock wave, the present study is aimed at complementing their study and investigating a dusty rarefaction wave. It should be noted, however, that in both studies the flow field was initiated by removing a diaphragm which at $t = 0$ was separating a high pressure from a low pressure zone. Therefore, basically in both cases the well-known shock tube problem is solved, but with opposite initial conditions as far as the dust presence is concerned.

2. Theoretical background

The conservation equations which govern the flow field developed behind shock or rarefaction waves, propagating into dust–gas suspension are discussed in detail in Igra, Elperin and Ben-Dor (1987). In the case of a one-dimensional planar flow they are:

$$\frac{\partial \rho}{\partial t} + \frac{\partial}{\partial x}(\rho u) = 0, \tag{1}$$

$$\frac{\partial}{\partial t}(\rho u) + \frac{\partial}{\partial x}(\rho u^2 + P) = -\frac{\sigma}{m} D, \tag{2}$$

$$\frac{\partial}{\partial t}\left[\rho\left(C_v T + \tfrac{1}{2}u^2\right)\right] + \frac{\partial}{\partial x}\left[\rho u\left(C_p T + \tfrac{1}{2}u^2\right)\right] = -\frac{\sigma}{m}(vD + Q), \tag{3}$$

$$\frac{\partial \sigma}{\partial t} + \frac{\partial}{\partial x}(\sigma v) = 0, \tag{4}$$

$$\frac{\partial(\sigma v)}{\partial t} + \frac{\partial}{\partial x}(\sigma v^2) = \frac{\sigma}{m} D, \tag{5}$$

$$\frac{\partial}{\partial t}\left[\sigma\left(C_m \theta + \tfrac{1}{2}v^2\right)\right] + \frac{\partial}{\partial x}\left[\sigma v\left(C_m \theta + \tfrac{1}{2}v^2\right)\right] = \frac{\sigma}{m}(vD + Q). \tag{6}$$

Eqs. (1)–(3) and (4)–(6) represent the conservation of mass, momentum and energy for the gaseous and the solid phases, respectively. The drag force acting on a solid particle is given by

$$D = 0.125\pi d^2\rho(u - v)\,|u - v|(0.48 + 28\ \mathrm{Re}^{-0.85}). \tag{7}$$

The rate of heat transfer between the two phases is given by:

$$Q = \pi d\mu C_p Pr^{-1}(T - \theta)(2 + 0.6\ \mathrm{Pr}^{1/3}\ \mathrm{Re}^{1/2}). \tag{8}$$

The equation of state of the gaseous phase, which is assumed to behave as a perfect gas, is:

$$P = \rho RT. \tag{9}$$

The notations used in eqs. (1)–(9) are as follows: ρ, u, P and T are the density, velocity, pressure and temperature of the gaseous phase, respectively; σ, v and θ are the spatial density, velocity and temperature of the solid phase, respectively; m is the mass of the solid particle and d is its diameter; C_v and C_p are the specific heat capacities at constant volume and constant pressure of the gaseous phase; C_m is the specific heat capacity of the solid particle; Pr, Re, R and μ are the Prandtl and Reynolds numbers, the gas constant and the gas dynamic viscosity, respectively; x is a spatial coordinate and t is the time.

The system of partial hyperbolic nonlinear differential equations (1)–(6) was solved numerically using the modified random-choice method with operator splitting technique. Details regarding the random-choice method can be found in Chorin (1976) and Sod (1977), and some specific details regarding the numerical scheme employed in the present study are given in Igra, Elperin and Ben-Dor (1987).

All calculations were performed using 750 mesh points. The average running time was 1200 seconds CPU on the CDC CYBER 180-840 computer.

3. Results and discussion

The numerical solution of eqs. (1)–(9) was performed for the following conditions:
dust mass loading ratio in the suspension, $\beta = 0$ 1, 4($\beta = \sigma_4/\rho_4$ at $t = 0$); diameter of dust particles, $d = 10$, 50 and 100 μm; dust specific heat capacity $C_m = 160$, 800, 4000 J/kg K.

The results are shown in a nondimensional form, i.e.,

$$\bar{P} = \frac{P}{P_1},\ \bar{T} = \frac{T}{T_1},\ \bar{u} = \frac{u\sqrt{\gamma}}{a_1},\ \bar{v} = \frac{v\sqrt{\gamma}}{a_1},\ \bar{\rho} = \frac{\rho}{\rho_1},\ \bar{\sigma} = \frac{\sigma}{\rho_1},\ \bar{x} = \frac{x}{L}\ \text{and}\ \bar{t} = \frac{a_1 t}{\sqrt{\gamma}L}$$

where index 1 stands for conditions at region 1 ($t = 0$, fig. 1), a is the local speed of sound, $\gamma = C_p/C_v$ and L is a characteristic length. The characteristic length L was chosen as 1 m. The diaphragm separating regions (1) and (4) was located at the center. All the numerical results shown in figs. 2–13 were obtained for the same initial conditions; they are:

$$\frac{P_4}{P_1} = 20,\quad \frac{T_4}{T_1} = 3.333,\quad P_1 = 1\ \text{atm},\quad T_1 = 300\ \text{K}.$$

The results presented in figs. 2–13 show the spatial variation of the flow properties at $\bar{t} = 0.158$ (unless specified otherwise on the figure).

The effect of the dust loading ratio on the suspension pressure is shown in fig. 2. It can be seen from fig. 2 that an increase in the dust loading ratio causes a larger pressure drop through the rarefaction wave, which, in turn, results in a stronger rarefaction wave. The weakest rarefaction wave (smallest pressure drop across the wave) is obtained for the dust-free gas case ($\beta = 0$). In this case the head and tail of the rarefaction wave (marked by H and T) are clearly

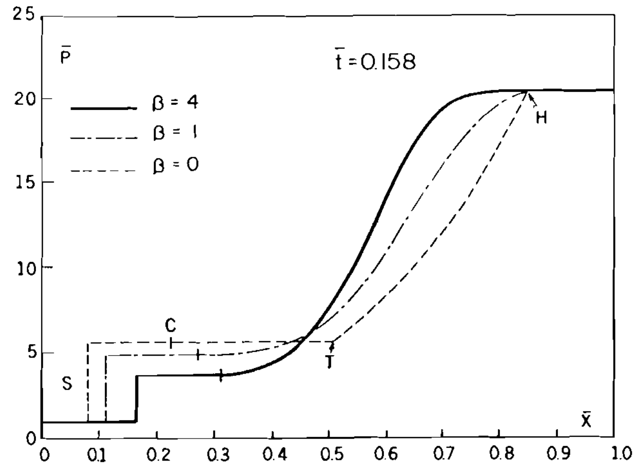

Fig. 2. The pressure distribution for three different values of loading ratio – β. (d = 10 μm, C_m = 800 J/kgK).

visible. The dust presence, however, smears out the head and tail of the rarefaction wave. Note that unlike the pressure profile for $\beta = 0$ where a kink clearly indicates the location of the tail, for $\beta = 1$ and $\beta = 4$ the kink is smeared out and the pressure gradient is continuous. In addition, it should be noted that the location of the head of the rarefaction wave, which propagates with the local speed of sound (i.e., a_4) is independent of the dust loading ratio. However, here again the location of the head is clearly visible when the gas is dust-free (there is a discontinuity in the pressure gradient) while for the case of dusty gas the discontinuity in the pressure gradient is smeared out. It is apparent from fig. 2 that changing the dust concentration in region (4) affects also the normal shock wave which propagates into the dust-free region, region (1), increasing the loading ratio reduces the strength of the shock wave and its velocity. The reason for the decline in the strength of the normal shock wave and its velocity, is that the flow pressure in region (2), behind the normal shock wave should be equal to that in region (3) since these two regions are separated by a contact surface. Thus the larger pressure reduction (stronger rarefaction) which is attained through the rarefaction wave, when the dust loading ratio in region (4) is increased, requires a smaller pressure jump across the normal shock wave i.e., a weaker shock wave. The location of the contact surface, which is not visible in fig. 2 since equal pressures exist on both of its sides, is marked on the pressure profiles for the readers' convenience. Fig. 3 shows the temperature distributions for $\bar{t} = 0.158$. Now the contact surface is clearly visible due to the temperature jump across it. The smallest temperature reduction is experienced by the rarefaction wave in the dust-free gas ($\beta = 0$). Increasing the dust loading ratio increases the temperature drop across the rarefaction wave, i.e., strengthens the rarefaction wave. Again in the case of a dust-free gas the head and tail of the rarefaction wave (marked by H and T in the figure) are clearly visible. The dust presence smears out the discontinuities in the temperature gradient and also affect the contact surface. In the case of a pure gas ($\beta = 0$) the contact surface appears as a planar surface with a sharp temperature jump across it. It should also be noted that while for a pure gas case the temperature changes inside the rarefaction wave linearly (see the temperature profile between H and T in fig. 3), in the case of a dusty gas, the temperature decreases behind the head of the rarefaction wave quite slowly, until it reaches a point where it experiences a steep drop.

The gas flow velocity distribution at $\bar{t} = 0.158$ is shown in fig. 4. The location of the contact surface, which cannot be seen in this figure since equal flow velocities exist on both of its sides is marked in each profile. It can be seen again that the weakest rarefaction wave is obtained in the case of a dust-free gas ($\beta = 0$) and that the strongest rarefaction wave is associated with the

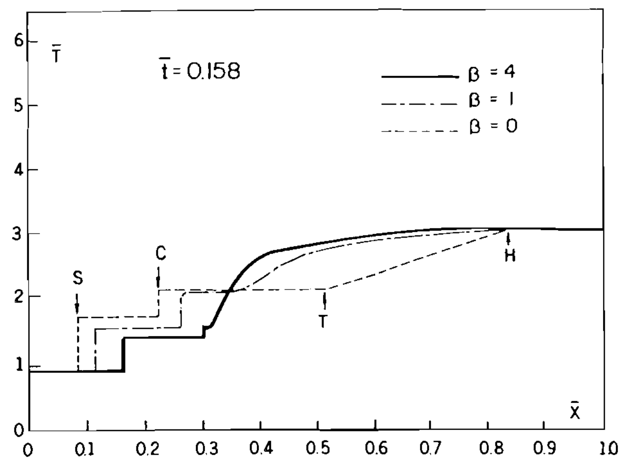

Fig. 3. The gas temperature distribution for three different values of loading ratio – β. ($d = 10$ μm, $C_m = 800$ J/kgK).

largest dust loading ratio ($\beta = 4$). The head and tail of the rarefaction wave are clearly visible in the pure gas case and are smeared in the dusty gas cases.

The effect of the dust particles diameter, on the suspension properties, is shown in figs. 5–9. Fig. 5 shows the pressure distribution for three different dust diameters, at $\bar{t} = 0.158$ and $\beta = 4$. It is apparent that the stronger rarefaction wave (i.e., larger pressure drop) is associated with the smaller dust particles ($d = 10$ μm), while the weaker one corresponds to the larger particles ($d = 100$ μm). Note that since the total mass of the dust particles in the suspension is the same for all three cases ($\beta = 4$), an increase in the dust diameter is associated with fewer particles in the suspension. Again, the location of the head of the rarefaction wave is independent of the dust presence. However, while for the larger particles ($d = 50$ and 100 μm) a discontinuity is obtained in the pressure gradient at the head of the rarefaction wave, for the smallest particles, $d = 10$ μm, this discontinuity is smeared out. The location of the contact surface, is again indicated on each of the three pressure profiles.

Fig. 6 shows the temperature distributions for $\bar{t} = 0.158$, $\beta = 4$ and three different diameters of the dust particles. Again the strongest rarefaction wave is associated with the smallest diameter of the dust particles (larger number of dust particles in the suspension). Unlike the previous case, the contact region is now clearly visible. Increasing the number of dust particles

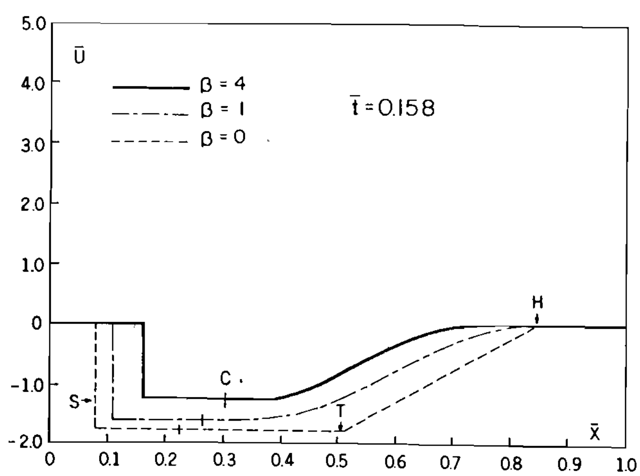

Fig. 4. The gas velocity distribution for three different values of loading ratio – β. ($d = 10$ μm, $C_m = 800$ J/kgK).

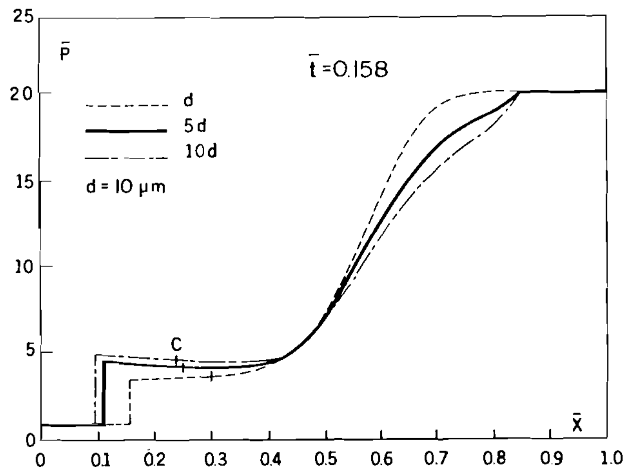

Fig. 5. The pressure distribution for three different values of dust particle diameter – d. ($\beta = 4$, $C_m = 800$ J/kgK).

in the suspension (by decreasing the diameter, d, in fig. 6 or increasing β in fig. 3) results in a sharp temperature peak at the contact region. It is evident from fig. 6 that the peak in the temperature at the contact surface is associated with the smaller particles. Since, as shown in fig. 8, (see subsequent discussion) the smaller particles are capable of catching up with the contact surface, it is plausible that their presence in the vicinity of the contact surface is the reason for this phenomenon. Note that when the diameter of the dust particles increases, the surface available for heat exchange, which is proportional to d^2, increases. However, since the total number of particles for a constant loading ratio β is proportional to d^{-3}, the total surface available for heat exchange varies as d^{-1}. This explanation might be further supported by the fact that the peak in the temperature vanishes as the diameter of the solid particles is increased.

Fig. 7 shows the flow velocity distributions for $\bar{t} = 0.158$, $\beta = 4$ and for three different diameters of the dust particles. It is apparent that increasing the dust particles diameter causes an increase in the flow velocity (note that the velocities in fig. 7 are negative and hence the lower curve corresponds to a higher absolute velocity) in a rarefaction wave (weaker rarefaction wave) which is in line with the results shown in fig. 5.

The dust velocity distributions are shown in fig. 8. As can be seen in fig. 8, the larger the particle is, the lower its velocity becomes (note again that the velocities are negative). This can

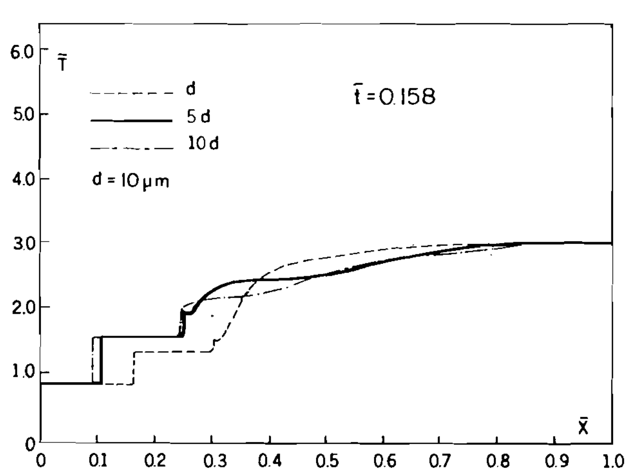

Fig. 6. The gas temperature distribution for three different values of dust particle diameter – d. ($\beta = 4$, $C_m = 800$ J/kgK).

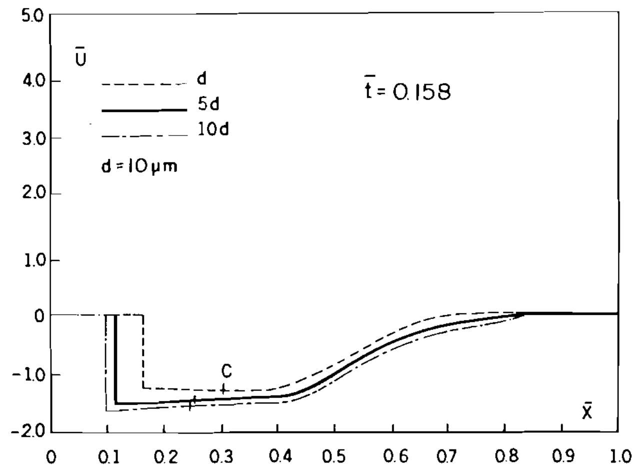

Fig. 7. The gas velocity distribution for three different values of dust particle diameter – d. ($\beta = 4$, $C_m = 800$ J/kgK).

be expected since the drag force which is responsible for accelerating the dust particles is proportional to d^2 while the particle mass is proportional to d^3. When comparing the velocities of the dust and the gas (figs. 8 and 7, respectively), it is apparent that longer times are required for the suspension with the larger particles to reach a kinematic equilibrium (equal velocities) with the carrying gas. The curves depicting the dust velocity (fig. 8) terminate at a a location where the dust spatial density becomes negligibly small. The location of the contact surfaces for the three cases at hand, as they appear in fig. 6, are added to fig. 8 and marked by C. It is obvious that the dust particles lag behind the contact surface. The larger the dust particle is the further it lags behind the contact surface. This observation is quite understandable since larger particles have a higher inertia and are, therefore, more difficult to accelerate.

The dust spatial density distributions are shown in fig. 9 for three dust particle diameters. As could be expected, the smaller dust particles penetrate further downstream the rarefaction wave since they have a smaller inertia and hence a higher velocity (see fig. 8). Thus, while the particles with diameter $d = 10$ μm can be found immediately behind the contact region (see figs. 8 and 9), the spatial density of the particles with the larger diameters becomes practically zero, long before they reach the contact region.

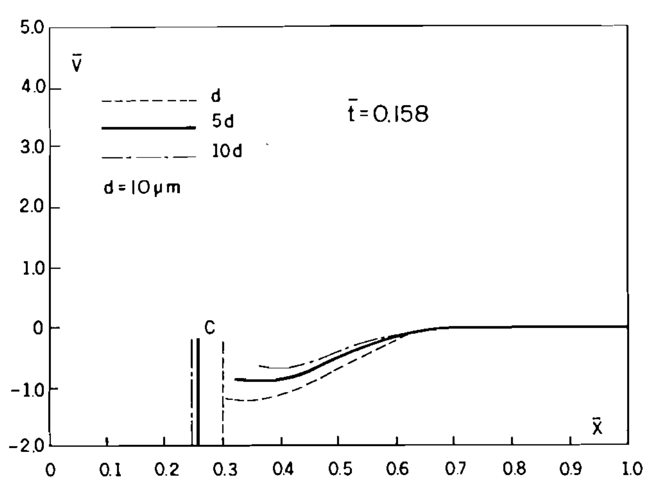

Fig. 8. The dust velocity distribution for three different values of dust particle diameter – d. ($\beta = 4$, $C_m = 800$ J/kgK).

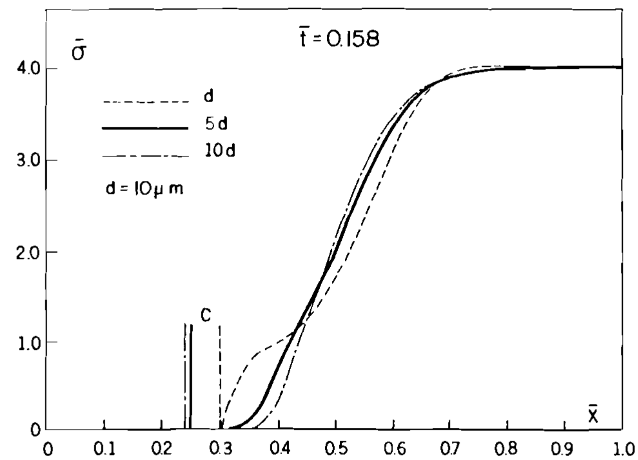

Fig. 9. The dust spatial density distribution for three different values of dust particle diameter – d. ($\beta = 4$, $C_m = 800$ J/kgK).

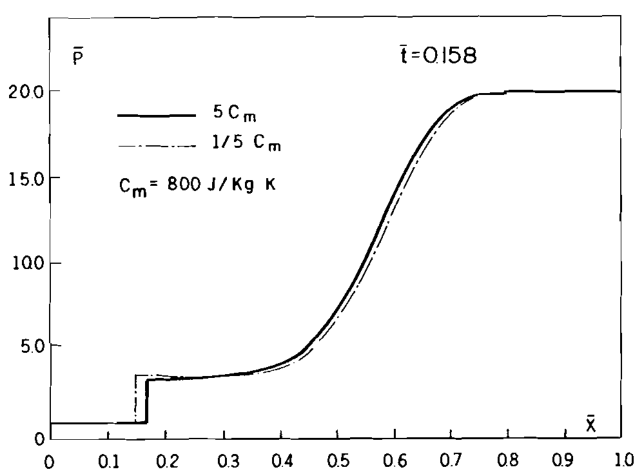

Fig. 10. The pressure distribution for two different dust specific heat capacities – C_m. ($d = 10$ μm, $\beta = 4$).

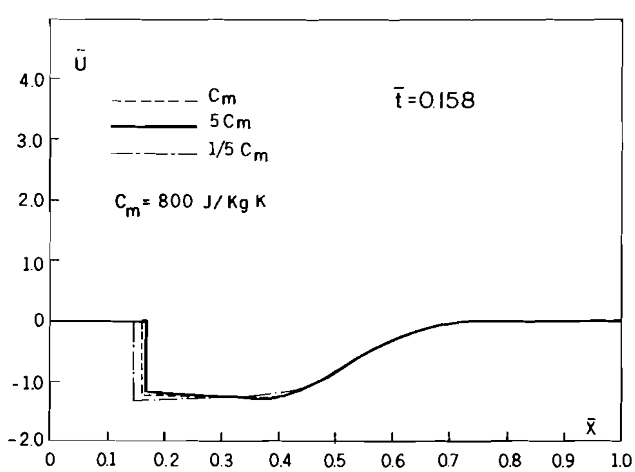

Fig. 11. The gas velocity distribution for three different dust specific heat capacities – C_m. ($d = 10$ μm, $\beta = 4$).

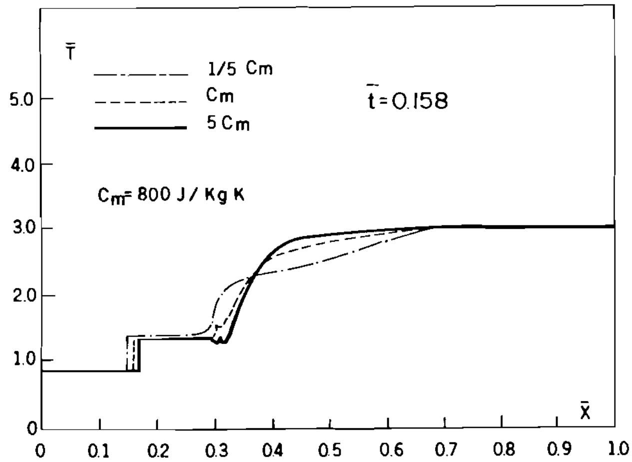

Fig. 12. The gas temperature distribution for three different dust specific heat capacities – C_m. ($d = 10$ μm, $\beta = 4$).

The dust particles specific heat capacity has a minor effect on the pressure and flow velocity throughout the rarefaction wave as can be seen from figs. 10 and 11, respectively. It has a definitely more pronounced effect on the temperature distribution. Fig. 12 shows that the weakest rarefaction wave is associated with the dust particles having the smallest specific heat capacity, and the strongest rarefaction wave is associated with the dust particles having the largest specific heat capacity (this is not quite clear from fig. 12, but was evident from the numerical results). Changing the dust specific heat capacity affects the heat transfer rate between the two phases and thereby the gas temperature inside the rarefaction wave. It is of interest to note that for the dust with the relatively low specific heat capacity ($C_m = 160$ J/(kg K)) the contact region is clearly visible. The temperature jump across this region is significantly reduced with increasing the value of C_m.

So far the spatial distributions of the suspension properties through the rarefaction wave at a given time ($\bar{t} = 0.158$) were discussed. In fig. 13 the pressure distributions at different times are shown. The propagation of the rarefaction wave into region (4), and the normal shock wave into region (1) is clearly visible. The dust presence ($\beta = 4$) smears the head and tail of the rarefaction wave more and more as time goes on.

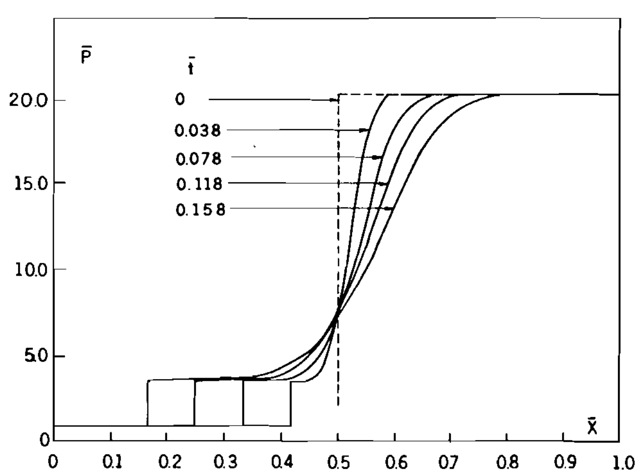

Fig. 13. The pressure distribution for five different times. ($\beta = 4$, $d = 10$ μm, $C_m = 800$ J/kgK).

3. Conclusions

The propagation of rarefaction waves into a dusty gas was studied numerically. It was shown that the dust presence has a significant effect on the developed flow field. Increasing the dust concentration increases the strength of the rarefaction wave and smears out the discontinuities in the gradients of the various flow properties at the head and the tail of the rarefaction wave. The dust particle diameter also affects the flow field in the rarefaction wave. The larger the particle diameter is (for a given dust mass loading ratio β), the weaker the rarefaction wave becomes. On the other hand, larger diameter particles move more slowly than smaller ones. The dust specific heat capacity has a minor effect on the suspension pressure and velocity but a more significant effect on the temperature distribution in the rarefaction wave. The smaller the specific heat capacity is, the lower the gas temperature, in the rarefaction wave, becomes.

Finally, it should be noted that unlike the case of a dust-free shock tube, where four flow regions are formed after the diaphragm is ruptured, namely; the pre-shock region (region 1), the post-shock region (region 2), the post-rarefaction region (region 3) and the pre-rarefaction region (region 4), where regions (2) and (3) are separated by a contact surface, in the present case of a dusty high pressure driver, the flow field consists of five flow regions. This is due to the fact that the flow field between the contact surface and the tail of the rarefaction wave (region 3) is subdivided into a dust-free and a dusty gas zone.

References

Bannister, F.K. and Mucklow, G.F. (1948) Wave action following sudden release of compressed gas from a cylinder, *Proc. Industrial and Mechanical Engineering, Vol. 159*, 269–300.

Chorin, A.J. (1976) Random choice solution of hyperbolic systems, *J. Comput. Phys. 22*, 517–533.

Igra, O. and Gottlieb, J.J. (1985) Interaction of rarefaction waves with area enlargements in ducts, *AIAA J. 23*, 1014–1020.

Igra, O., Elperin, T. and Ben-Dor, G. (1987) Blast waves in dusty bgases, *Proc. Roy. Soc. London, A414*, 197–219.

Marble, F.E. (1970) Dynamics of dusty gases, *Ann. Rev. Fluid Mech. 2*, 397–466.

Miura, H. and Glass, I.I. (1982) On a dust-gas shock tube, *Proc. Roy. Soc. London A382*, 373–388 (see also UTIAS Report No. 250, 1980).

Oppenheim, A.K., Urtiew, P.A. and Laderman, A.J. (1964) Vector polar method for the evaluation of wave interaction processes, Archiwum Budowy Maszyn (*The Archive of Mechanical Engineering), Vol. XI*, 441–495.

Rudinger, G. (1969) Nonsteady Duct Flow: Wave Diagram Analysis (Dover Publications, New York).

Rudinger, G. (1973) Wave propagation in suspension of solid particles in gas flow, *App. Mech. Rev. 20*, 273–279.

Sod, G.A. (1977) A numerical study of a converging cylindrical shock, *J. Fluid Mech. 83*, 785–794.

Soo, S.L. (1967) Fluid Dynamics of Multiphase Systems (Blaisdell Publishing, Waltham Mass).